Electrodeposited copper micropillar surfaces with pulse reverse voltammetry for enhanced heat dissipation

Jayce JW Cheng[1*], FengXia Wei[1], Sing Yang Chiam[1]

[1] Institute of Materials Research and Engineering, Agency for Science, Technology and Research, 2 Fusionopolis Way, Singapore 138634

*Corresponding Author

Abstract

Microstructured metal coatings are promising for many commercial applications due to their robustness, high thermal and electrical conductivity, and interesting functionalities. In particular, copper electrodeposition has been widely studied due to its low cost and scalability while maintaining excellent material quality. Here, we use pulse electrodeposition to simultaneously monitor and generate copper microstructures on copper and aluminum surfaces. By rapidly applying forward and reverse potentials, we identify a key metric – the ratio of deposition to etching – that has a characteristic temporal profile for four different growth regimes: thin film, pyramids, micropillars, and dendrites. We explore the parameter space by varying forward voltage between 100 – 500 mV, and added chloride between 100 – 1000 ppm, to transition the microstructure between these four growth regimes, allowing us to obtain the desired surface structure. With this capability, we deposit micropillar arrays on large-area copper and aluminum heatsink surfaces, yielding performance enhancements of 10% and 4% respectively, showing that such coatings are promising for thermal management applications.

Keywords: Copper electroplating, pulse electrodeposition, micropillars, thermal management, heatsink

Introduction

Microstructured metal surfaces have been widely exploited in scientific and commercial applications due to their high electrical conductivity, thermal conductivity, and varied surface states and functionalities. They are mechanically robust, stable at high temperatures, and are easily integrated into existing scalable and cost-effective industrial processes. In particular, functional microstructured copper coatings have been used for thermal management[1-3], carbon dioxide reduction[4-5], superhydrophobic surfaces[2, 6-7], and electrical interconnects[8-9].

Electrodeposition of thin film copper coatings has been widely studied and many optimized processes exist for the high throughput, large scale deposition of high quality copper coatings with excellent adhesion to a myriad of conductive substrates[10-11]. Material properties such as grain size, grain orientation, and interfacial properties can be tuned through careful choice of starting electrolyte (acid sulfate, cyanide, halide, *etc*.)[11], additives (accelerator, suppressor, leveler, brightener)[8, 12-13], and electrodeposition parameters[14]. The affinity of halides to adsorb to copper facets[13], and in particular chloride[15], makes them useful tuning agents. The sensitivity of copper coating morphology to each of these inputs results in a massive parameter space that has yet to be fully explored, making this material system interesting for functional applications.

Classical thin film copper electrodeposition focuses on producing mirror-finish surfaces with high hardness and good adhesion for structural applications. The acid-copper sulfate chemistry is utilized for its 'throwing power' at low pH – the ability of an electrolyte to conceal underlying roughness and micron-scale defects[11] by increasing the copper adatom or cuprous ion diffusion length above the lengthscale of surface roughness, allowing adatoms/ions to move to regions of high surface energy density (low curvature) before incorporation, thereby concealing regions with high curvature[16]. Conversely, dendrite formation is characteristic of morphological instability,

where regions of high curvature are emphasized due to concentration of charge in the electrode and of chemical species in the electrolyte with low effective mobility (diffusion-limited)[17]. By manipulating applied potential, electrolyte composition and agitation, and adsorbed species, this tradeoff between reaction rate and mass transport to the electrode can be exploited to microstructure the surface in a single step, bottom-up process. Numerous previous studies have utilized top-down approaches to generate copper microstructures, ranging from plating through alumina[18-19] or polymer templates[2, 20], or with lithographic techniques[6, 21], but such approaches are not amenable to high-throughput electroplating processes.

Pulse voltammetry refers to characterization techniques that study the response of an electrochemical system to an instantaneous perturbation; chronoamperometry tracks the change in current after a potential step. After an overpotential is applied, the transient response as the system relaxes to an equilibrium state can reveal information about mass transport ($I \sim t^{-\frac{1}{2}}$)[22], surface reaction rate ($I \sim t^{\frac{1}{2}\ to\ \frac{3}{2}}$)[15], and other processes such as double layer charging ($I \sim e^{t}$)[23] and adsorption of surface species[22]. However, using pulse voltammetry as an electrodeposition technique is interesting because rapid pulses can ensure that the system always stays at or near to the kinetic limited regime[24-25]. Allowing the concentration of reactants near the electrode to re-equilibrate between pulses means that the electrode reaction is no longer mass-transport limited, and hence independent of external conditions such as electrolyte volume, agitation, distance between electrodes, *etc*. which complicate the deposition process. This technique thus provides an extra handle to tune the material properties[26], being used to generate high hardness nanocrystalline[24, 27-28] and nanotwinned[29-30] copper and also commercial wafer-scale metallization processes[31-32].

Here, we utilize pulse electrodeposition to simultaneously monitor and generate novel copper microstructures on copper and aluminum substrates. Working with the ubiquitous acid-copper sulfate chemistry, we first explored the parameter space by varying forward step voltage from 100 – 500 mV with constant backward step voltage and pulse duration, as well as changing the chloride concentration from 100 – 1000 ppm, to obtain the dependence of surface morphological evolution on electrolyte and electrodeposition parameters. Transition between surface growth morphologies (1) thin film, (2) pyramids, (3) micropillars and (4) dendrites was observed in this parameter space, providing multiple handles for tuning the coating microstructure. Supported by a time series study, we postulate that the unique star-shaped prismatic cross-sections on copper micropillar arrays arises from differential deposition/etch rates on Cu‹100› *vs*. Cu‹110› facets in the presence and absence of chloride, accentuated by the cyclic nature of pulse electrodeposition. Finally, having developed a way to tune the electrodeposited microstructure, we fabricated micropillar coatings on copper and aluminum heatsinks, obtaining 10% and 4% performance enhancements in heat flux respectively, showing that such coatings are promising for thermal management applications.

Experimental details

Electrodeposition was carried out in a three-electrode system with copper foils (99.999% pure) as both working and counter electrodes. The working electrode was masked with Kapton tape to define a circular planar surface of 0.283 cm^2. The electrodes were cleaned by ultrasonicating for 10 min each in acetone and IPA, followed by oxide removal with 1 min soak in glacial acetic acid. A double junction Ag/3.0M KCl/3.0M KNO_3 reference electrode (Metrohm) was used to avoid contamination of the electrolyte with chloride ions. Chloride concentration was varied between 0 to 1000 ppm by adding 37% HCl to 125 ml of electrolyte composed of 0.5M sulfuric acid and

either 0.3M or 0.5M copper (II) sulfate anhydrous (99.99%) in 18.0 MΩ MilliQ deionized water (All chemicals from Sigma-Aldrich). The electrolyte was not stirred during deposition.

Chronoamperometry experiments were carried out using a Metrohm Autolab (PGSTAT302N) equipped with high-speed amplifier configuration (125 kHz; 8 µs ramp time) to apply the pulsed voltage profiles shown in Figure 1a. Following IUPAC convention, cathodic (Cu^{2+} reduction, *i.e.* deposition) and anodic (Cu oxidation, *i.e.* etching/dissolution) potentials are plotted as negative and positive respectively. Cyclic voltammetry and Tafel analysis in 0.3M Cu/0.5M sulfuric acid were performed to validate the system; more details are given in Supporting Figure S1. The forward (deposition) step height was varied from 100 to 500 mV *vs*. open circuit potential (OCP ranged from 75 to 60 ± 5 mV *vs.* Ag/3M KCl/3M KNO_3 with increasing chloride due to polarization[33]) in 100 mV steps while the backward (etching/dissolution) step height and duration was kept constant; the current was sampled 4× in each step (Figure 1a and b). The deposited films were then rinsed with DI water, dried with compressed air, and left overnight in a 60^{o}C oven to fully remove water from the microstructure. Top-down scanning electron microscopy (SEM) and electron dispersive spectroscopy (EDX) analysis were carried out in a JEOL 7600F, and cross-section SEM was carried out using an FEI Helios Nanolab 600. Heat dissipation measurements were performed in a purpose-built heatsink testing setup as described in the Supporting Information.

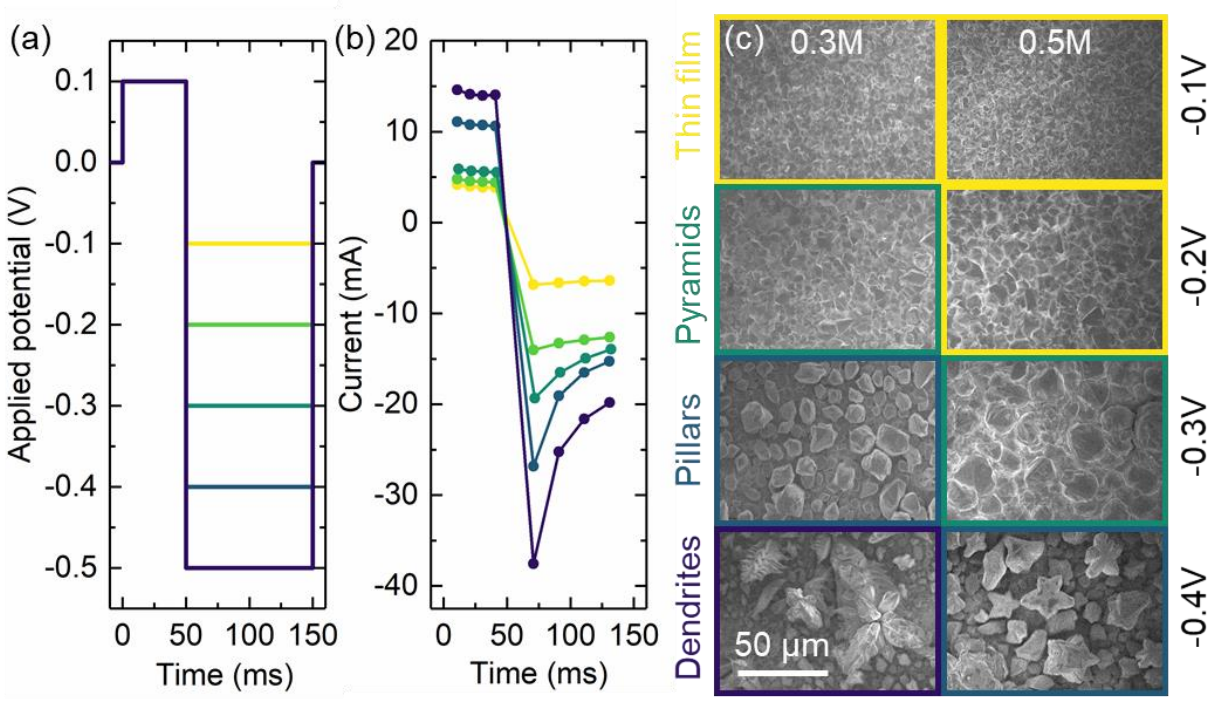

Figure 1. (a) Applied potential *vs.* OCP and (b) Measured current *vs*. time for a single pulse in 0.3M Cu electrolyte with 200ppm added chloride, displaying diffusion-limited response. This current profile was measured at t = 750s during a 1500s electrodeposition. (c) Representative top-down SEM images of electrodeposited films at varying applied potential in 0.3M and 0.5M Cu electrolyte both with 200ppm added chloride. The type of microstructure obtained for each condition is labelled by color.

Results and discussion

Pulse voltammetry electrodeposition yielded polycrystalline copper thin films with microstructures that transitioned from the 2D to 3D growth mechanism (*i.e.* from pyramids to pillars) within the parameter space of this study (Figure 1c and Supporting Figure S2). All depositions were carried out for 1500s. In control samples (no added chloride) this transition took place between 300 – 400 mV for both 0.3 and 0.5M copper concentration. While adding chloride did not change the transition potential in 0.5M electrolyte, adding chloride to 0.3M electrolyte had a stronger effect on morphology, shifting the transition to lower applied potential between 200 – 300 mV – the well-known accelerating effect of chloride is obvious here[33-34]. Depositions carried

out at 500 mV potentials resulted in uncontrolled dendrite growth and fragile films that disintegrated during rinsing, and could not be imaged. Thin films deposited with between 100 – 300 mV and 700 – 1000 ppm chloride formed a top layer of copper (II) chloride crystals[33], which were easily identifiable through their triangular shape and also confirmed using EDX (Supporting Figure S3). As expected for deposition in acid copper electrolye with chloride additives[35], copper thin films deposited between 100 mV and 300 mV show increases in grain size and surface roughness with applied potential for all samples.

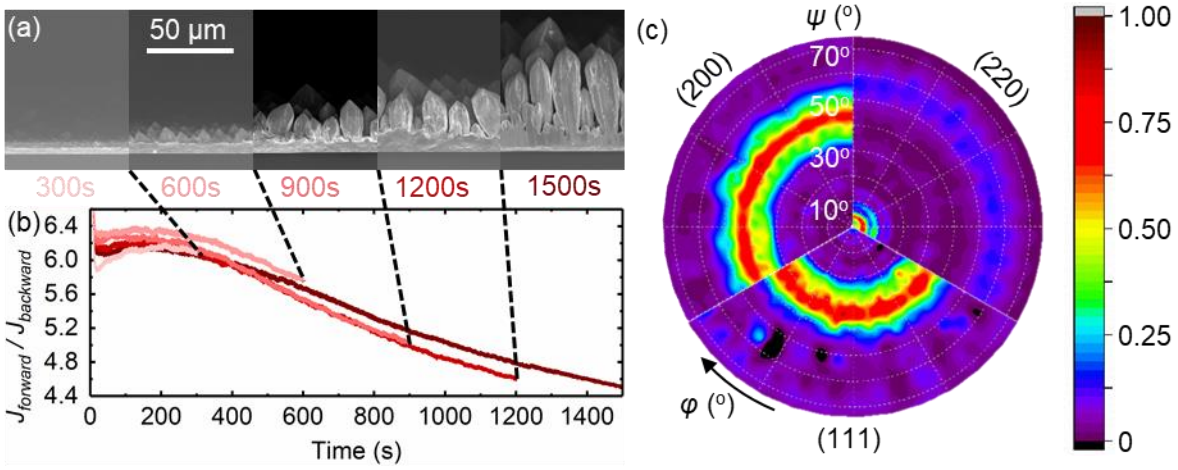

Figure 2. (a) Cross-section SEM images of electrodeposited copper microstructures on silicon substrate on top of a 100 nm PVD Ta/900 nm PVD Cu seed layer, with increasing deposition time. Electrodeposition was carried out at 400 mV applied potential in 0.5M Cu electrolyte with 200 ppm added chloride. (b) The corresponding $R_{\frac{f}{b}} = \frac{J_{forward}}{J_{backward}}$ *vs.* time showing characteristic profiles for each step of microstructure evolution. (c) Wulff plots for Cu(200), (220), and (111) crystallographic directions. For brevity, 120° sectors of each pole figure are shown, as they are isotropic in φ (radial coordinate); full figures in Supporting Information. ψ (azimuthal coordinate) and normalized intensity (colorbar) are shown on the figure.

Cross-sectional SEM on a time series was performed to confirm that vertically aligned microstructures had indeed been deposited (Figure 2a), and also to monitor the surface evolution at different deposition times. Deposition was carried out at forward potential 400 mV, in 0.5M copper electrolyte with 200 ppm chloride, for increasing 300s time intervals on substrates

comprising Si/100 nm PVD Ta/900 nm PVD Cu; the samples were then cleaved for SEM inspection. Despite the smaller grain size of PVD Cu seed layer, as compared to the previously used copper foils, the microstructure generated was remarkably similar and displayed a 2D to 3D transition between 600 – 900s deposition time. XRD pole figure analysis (Figure 2c and Supporting Figure S5) showed that deposited films were highly ‹110› textured normal to the substrate, with the expected bands at $\psi = 35^{o}$ and $\psi = 45^{o}$ from the (111) and (100) reflections respectively[26-27]. Deposition time of 300s formed a ~4 μm thin film with a rough surface; further deposition up to 600s formed angular pyramids on the thin film surface (also observed by Nikolić *et. al.*[36]). Micropillars were obtained after 900s and further deposition caused the micropillars to grow vertically up to ~40 μm height after 1500s. Micropillar height increased linearly after nucleation, which was confirmed by the total charge (Supporting Figure S4a). Micropillars displayed broadening towards the top, with shorter micropillars distributed amongst longer micropillars. This distribution is characteristic of diffusion-limited growth, where longer micropillars grow at the expense of shorter micropillars by consuming limited reactants[37]. This can be seen in the current density transients (Supporting Figure S4b) for each pulse, which show that the system grows increasingly diffusion-limited as growth proceeds and the surface area increases while bulk copper concentration remains constant. In such a growth regime, the areal density of micropillars decreases with time while individual micropillars increase in diameter.

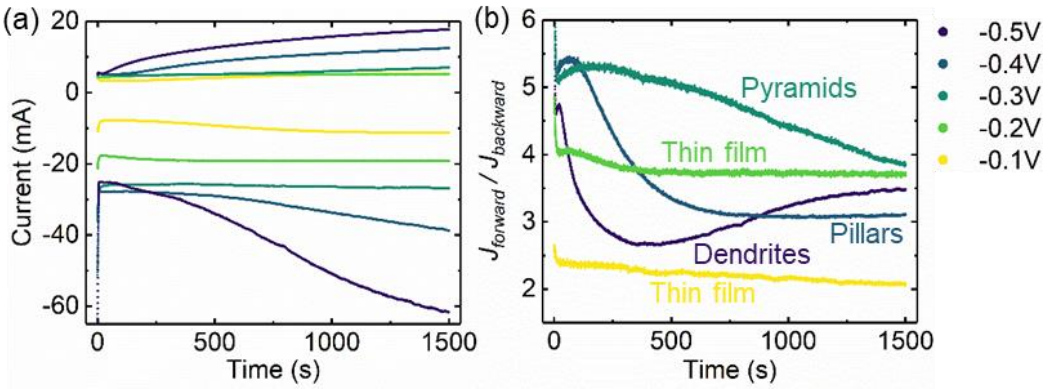

Figure 3. (a) Current density *vs*. time (*J-t*) plot for deposition at applied potentials between 100 – 500 mV in 0.5M Cu electrolyte with 200ppm added chloride and (b) $R_{\frac{f}{b}} = \frac{J_{forward}}{J_{backward}}$ *vs*. time for the same electrodeposition illustrating characteristic profiles for the different types of microstructure evolution as labelled.

From the electrochemical perspective, the transition from thin film to micropillar growth can be derived from the chronoamperometry (*J-t*) plots. Inspecting the *J-t* plots for both 0.3M and 0.5M electrolyte (Figure 3a and Supporting Figure S6a) does not reveal any special features that differentiate micropillar growth *vs*. thin film growth – there is no significant increase in the slope of the forward deposition current before and after the transition potential that could be attributed to a large increase in surface area[16]. While uncontrolled dendrite growth is clearly reflected in a steep slope, the forward deposition curves for micropillar samples are indistinguishable from thin film samples. Notably, it is the variation in the ratio of forward to backward current density ($R_{\frac{f}{b}} = \frac{J_{forward}}{J_{backward}}$) with time that shows a distinct profile in the case of micropillar growth (Figure 3b and Supporting Figure S6b). This is unsurprising since we expect the relative rate of deposition *vs*. etching to be critical in propagating morphological instability. Consider a representative set of results deposited from 100 – 500 mV overpotential in 0.5M copper electrolyte with 200 ppm added chloride (Figure 3a, SEM in Figure 1c). In the case of thin film growth at 100 and 200 mV, following an initial induction period, $R_{\frac{f}{b}}$ does not vary significantly with time for the rest of the

growth period. This implies that the net rate of material deposition remains the same throughout. However, for growth of thin films with pyramidal tops (300 mV overpotential), $R_{\frac{f}{b}}$ falls continuously with time, indicating that the pyramids are possible intermediates in formation of this microstructure, *i.e.*, they would develop into micropillars if the deposition time was extended. For micropillar growth (400 mV overpotential), $R_{\frac{f}{b}}$ falls precipitously in the first 600s before leveling out, indicating that there are two growth regimes in micropillar growth: (1) formation or nucleation of the micropillars, likely *via* pyramid structures, and subsequent (2) vertical growth of the micropillars. Finally, dendrite growth at 500 mV overpotential goes through a similar nucleation step, with a steep increase in etch rate, but the deposition rate subsequently recovers as the microstructure grows uncontrollably due to morphological instability. This results in a time profile where $R_{\frac{f}{b}}$ increases with time instead of leveling out, thus distinguishing it from $R_{\frac{f}{b}}$ for micropillar deposition. These four different types of microstructure (thin film, pyramidal, micropillar, dendritic) are easily identified from their characteristic change in $R_{\frac{f}{b}}$ for all the other deposition conditions in the presence of chloride. This is also confirmed by the time series electrodepositions on PVD copper seed layer on Si (Figure 1b) which clearly correlate the evolution of $R_{\frac{f}{b}}$ during the transition between each type of microstructure. Monitoring $R_{\frac{f}{b}}$ is thus an excellent metric to gauge the real-time state of the surface during deposition, and also provides a way of confirming the type of microstructure obtained.

We observe a distinct difference between the morphology of copper micropillars generated with and without added chloride –microstructures with rounded edges are generated in the absence of chloride, but addition of chloride ions causes micropillars to have sharp edges and angular sides

(Figure 4). A large proportion of micropillars also display the results of preferential etching on certain facets, which manifests as star-shaped prismatic cross-sections. Star-shaped prisms with three to five sides are observed because the micropillars are polycrystalline and therefore do not reflect the copper crystal structure. Nevertheless, the appearance of preferentially etched facets only in the presence of chloride ions could reflect the tendency of halides to adsorb to copper facets on which their monolayer spacing aligns favorably with the underlying copper crystal structure, promoting a lower energy configuration. The effect of halide adsorption on ledge growth in Cu (100) and (111) facets[34, 38-39] has been well documented in the literature: in-situ STM by Magnussen and Broekmann show that the accelerating effect of chloride ions arises from promoting high energy edge configurations resulting in the formation of angular ledges[34, 40].

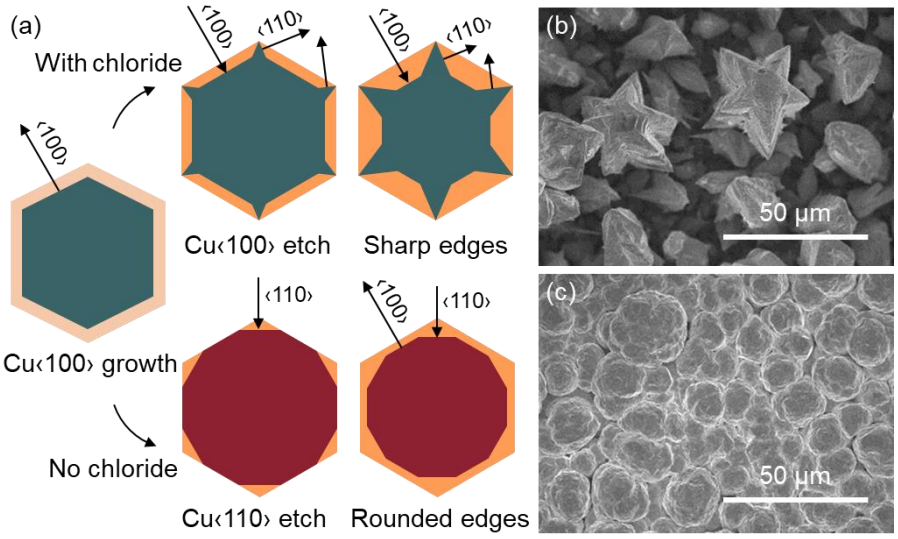

Figure 4. (a) Mechanism of microstructure evolution with and without added chloride. Top-down SEM images of copper microstructure deposited in 0.5M Cu electrolyte at 400 mV with (b) 1000ppm and (c) 0 ppm added chloride, images at same magnification.

Since the micropillars are highly ‹110› textured normal to the surface, we postulate that the obtained microstructure is due to adsorbed chloride emphasizing the morphological instability

between the Cu (100) and (110) facets[27] which form the pillar sidewalls. The formation of star-shaped cross-sections from alternating deposition/etch processes has previously been demonstrated in copper nanocrystals[4] and zinc oxide nanowires[41], with preferential removal of high energy Cu (110) and ZnO $(10\bar{1}0)$ facets respectively. Cu (111) facets are the fastest growing and are quickly buried under other lower energy facets. Previous studies have shown that Cu (110) planes are more susceptible to etching than (111) and (100) planes due to their lower atomic density and high number of dangling bonds[4, 26]. However, the addition of chloride, which has the most favorable adsorption to the (100) facet as a c(2 × 2) adlayer, reverses the relative stabilities of the (100) and (110) facets due to its accelerating effect[40, 42]. As can be seen in the mechanism schematic in Figure 4a, facets on which adatom incorporation are favored have high energy (more dangling bonds), and are therefore also subjected to higher etch rates than other lower energy facets, which are more stable to material removal. This causes (100) surfaces to be removed, exposing more stable lower-energy (110) facets[26-27] and producing the angular, star-shaped surfaces seen in our microstructure. In the absence of chloride, (110) has a higher energy and its removal results in the rounded edges obtained in the microstructure[20]. Electrochemically, we recall that the characteristic of micropillar growth is the steep decrease in $R_{\frac{f}{b}}$ (deposition rate *vs*. etch rate), also showing that material removal is critical for producing the angular microstructures. Addition of chloride coupled with deposition/etch cycles thus provides a way to mediate between the Cu(100) and (110) facet energies, thereby allowing us to tune the microstructure by affecting the type of facet exposed to solution.

We were also able to characterize mass transport to and from the electrode as 10000 forward and reverse pulses were applied to the working electrode over the course of 1500s and the current response was sampled during each ~ 100 ms cycle, essentially conducting thousands of pulse

voltammetric measurements and providing us detailed information about how mass transport at the electrode changes with time (Figure 1b). By fitting the current density transients from each pulse to the Cottrell relationship ($I = k_i t^{-\frac{1}{2}}$, further details in Supporting Figure S7), we were able to derive the forward and backward mass transport rate constants (k_f and k_b). The magnitude of the rate constants reflects how fast the system can respond to the voltage step, *i.e.*, higher values of k_f and k_b mean a lower ability of mass transport to deliver sufficient reactant to the electrode surface. The system is thus less limited by Faradaic response and more diffusion-limited. During deposition, k_f increases with applied voltage as the deposition current increases due to increased surface area, and mass transport is unable to deliver sufficient reactant to the surface. The accelerating effect of chloride on the forward reaction can also be seen in increasing k_f with higher chloride concentration. The presence of chloride has a strong effect on material removal from the electrode as evidenced by the large increase in k_b after adding 100 ppm of chloride. Similar to deposition, etching also becomes more diffusion-limited as the surface evolution proceeds and etching current increases due to larger surface area. Notably, the increased etch rate that causes the characteristic $R_{\frac{f}{b}}$ profile in micropillar growth can also be seen in the mass transport measurements, which feature initially low material removal rates that increase as the micropillars are generated.

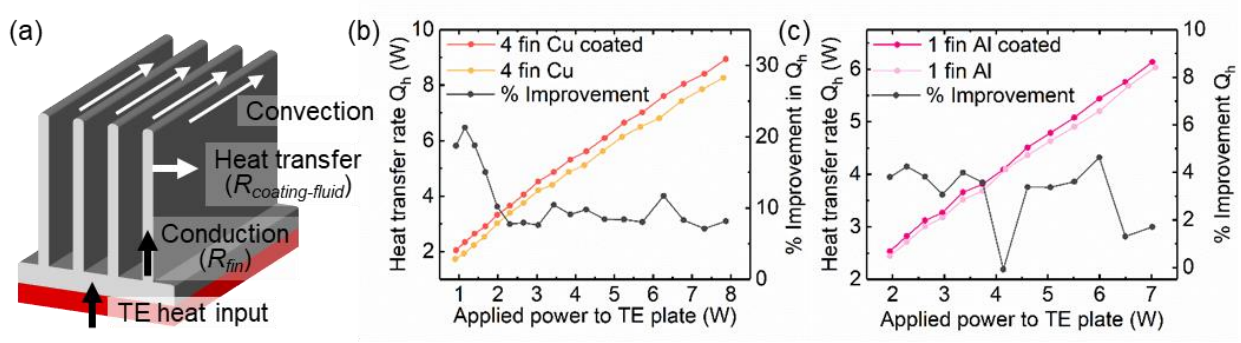

Figure 5. (a) Schematic of heat flow through a heatsink mounted on a thermoelectric (TE) Peltier heat pump, with transverse fluid flow through cooling fins. (b) Copper and (c) aluminum heatsink performance showing heat transfer rate Q_h through the TE plate *vs.* applied power, as well as % improvement in Q_h at different power for coated heatsink fins.

Having developed the capability to deposit micropillar arrays, we applied them to a heatsink surface to investigate if the increased surface area would enhance heat dissipation (Figure 5a). While heatsinks are typically made of lightweight aluminum which has moderate thermal conductivity, solid copper heatsinks provide better thermal management performance due to their higher heat conductivity. However, copper is heavy and thus unsuitable for mobile applications, which limits their widespread adoption. An electrodeposited copper micropillar coating on aluminum substrate would therefore combine the advantages of both materials, while being a scalable and low cost synthesis method suitable for coating heatsinks with large surface areas. Improved performance on copper heatsinks would also reduce the amount of copper needed, saving weight in mobile applications.

Copper and aluminum sheets with dimensions 16 × 40 mm were coated on both sides with copper micropillar films deposited at 300 mV from 0.3M copper electrolyte with 200 ppm added chloride for 1500s. A purpose built heatsink testing apparatus (Supporting Figure S8) was then used to measure the heat flux through coated and uncoated heat sinks with either one or four fins. The micropillar coatings were indeed able to improve heat dissipation from the heatsinks, showing the

best thermal performance improvements of ~10% on 4-fin copper and ~4% on 1-fin aluminum heatsink fins (Figure 5b and c).

The performance differences can be justified by considering the heat transfer rate between the Peltier plate and cooling fluid (Figure 5a), modeled as additive series resistances R_{fin}, $R_{fin-coating}$, and $R_{coating-fluid}$. R_{Cu} and R_{Al} are the bulk thermal conductivities of copper and aluminum (385 and 232 $Wm^{-1}K^{-1}$ respectively at 298 K)[43], while literature values for R_{Cu-Cu} and R_{Cu-Al} for flat milled surfaces are 5.5×10^4 and 4.2×10^4 $Wm^{-2}K^{-1}$ respectively[44]. Although R_{Cu-Al} is 20% less than R_{Cu-Cu}, we note that R_{Cu-Al} was measured for heat transfer from copper to aluminum, while our fins transfer heat from aluminum substrate to copper micropillar coating. Given that R_{Cu} is almost half of R_{Al}, interfacial heat transfer from aluminum to copper is likely to be fast compared to heat conduction through the fin bulk itself. Lastly, R_{Cu-air} (heat transfer from coating to air) is the same in both coated aluminum and copper fins since the electrodeposition was identical. However, R_{Cu-air} is different between a microstructured surface and a flat polished surface because of friction: a textured surface has a higher surface roughness and thus a lower fluid flow rate, which is detrimental to heat dissipation by convection. This common issue in heatsink design means that any surface texturing involves a tradeoff between higher surface area and slower fluid flow, which makes tuning of the microstructure dimensions and morphology critical for performance enhancement.

This is clearly illustrated in the differences between the 4- and 1-fin heatsinks. In the 4-fin heatsink, specific R_{Cu-air} is lower than in the 1-fin heatsink because of the high surface area, *i.e.* heat dissipation from the coating to air is fast. Because fluid flow through the multiple fins is already slow, there is no appreciable effect of friction from the coating. The limiting factor for heat transfer

is then R_{Cu} *vs.* R_{Al}. The coated 4-fin copper heatsink thus shows a large performance enhancement because heat conduction through the fins from the Peltier plate to the coating is taking place quickly. However, the coated 4-fin aluminum heatsink does not show any increase in heat transfer rate because conduction through the aluminum fin is the limiting factor and the coating is unable to make an appreciable difference to heat dissipation (Figure 5c). In contrast, specific R_{Cu-air} is much higher in the 1-fin than in the 4-fin heatsink. Fluid flows easily past the 1-fin heatsink and therefore texturing the surface significantly decreases the flow rate. Since heat conduction through the copper fin is the same in both coated and uncoated substrates, there is no performance enhancement in 1-fin copper heatsinks (Figure 5b). The performance enhancement in coated 1-fin aluminum heatsinks arises because conduction through the aluminum is no longer the limiting process, and thus the coating shows a modest improvement in heat dissipation to the fluid over the flat surface.

Conclusion

We have demonstrated control over the morphology of a copper micropillar array using pulse electrodeposition in a commercially available electrolyte on off-the-shelf copper and aluminium foil substrates. By investigating the electrochemical response of the growing metal surface to varying applied voltage and chloride concentration, we were able to simultaneously monitor and generate a spectrum of microstructures, passing through growth regimes for thin film, pyramids, micropillars, and finally dendritic structures. Adding chloride to the electrolyte above 100 ppm concentration substantially changed the surface morphology from rounded to angular profiles. Chloride also emphasized 3D growth, shifting the micropillar growth regime to lower applied potentials. Micropillar arrays were deposited at applied potentials of 300 mV and 400 mv in 0.3M and 0.5M Cu electrolyte respectively. We were able to identify $R_{\frac{f}{b}} = \frac{J_{forward}}{J_{backward}}$ as a key metric for

monitoring surface evolution as each microstructure yielded characteristic curves that could be used to identify them. From this, it was surmised that the generation of star-shaped prismatic micropillars was heavily dependent on the deposition *vs*. etch rate on Cu (100) *vs*. (110) facets, in the presence and absence of chloride. With the ability to control morphology, we deposited copper micropillar arrays on aluminum and copper heatsink fins and showed 10% and 4% enhancement in heat flux respectively. Copper micropillar arrays are thus promising for thermal management applications, but could also be interesting in applications such as carbon dioxide reduction and photovoltaic devices. Further studies to investigate more closely the influence of applied potential (*e.g.* in smaller potential steps, varying reverse potential, varying pulse width) and the influence of additives could yield even better control of the morphology and generate more novel structures.

Supporting Information

Supporting information contains details regarding electron micrographs of deposited thin films, EDX spectroscopy, XRD crystallographic pole figures, chronoamperometry plots, and the heatsink characterization setup.

Conflict of Interest Declaration

The authors declare no competing financial interest.

Corresponding Author

Address correspondence to: jayce_cheng@imre.a-star.edu.sg

Author Contribution

J. Cheng and S. Y. Chiam designed and performed electrochemical deposition and microscopy experiments. F. Wei performed XRD characterization and results analysis.

Funding Sources

This research was supported by the A*STAR Science & Engineering Research Council under the Defect Science Program.

Bibliography

1. Jung, S. M.; Preston, D. J.; Jung, H. Y.; Deng, Z.; Wang, E. N.; Kong, J., Porous Cu Nanowire Aerosponges from One-Step Assembly and their Applications in Heat Dissipation. *Adv Mater* **2016,** *28* (7), 1413-9.
2. Barako, M. T.; Isaacson, S. G.; Lian, F.; Pop, E.; Dauskardt, R. H.; Goodson, K. E.; Tice, J., Dense Vertically Aligned Copper Nanowire Composites as High Performance Thermal Interface Materials. *ACS Appl Mater Interfaces* **2017,** *9* (48), 42067-42074.
3. Barako, M. T.; Gambin, V.; Tice, J., Integrated nanomaterials for extreme thermal management: a perspective for aerospace applications. *Nanotechnology* **2018,** *29* (15), 154003.
4. Wang, Z.; Yang, G.; Zhang, Z.; Jin, M.; Yin, Y., Selectivity on Etching: Creation of High-Energy Facets on Copper Nanocrystals for CO2 Electrochemical Reduction. *ACS Nano* **2016,** *10* (4), 4559-64.
5. Zhu, Q.; Sun, X.; Yang, D.; Ma, J.; Kang, X.; Zheng, L.; Zhang, J.; Wu, Z.; Han, B., Carbon dioxide electroreduction to C2 products over copper-cuprous oxide derived from electrosynthesized copper complex. *Nat Commun* **2019,** *10* (1), 3851.
6. He, Z.; Zhang, Z.; He, J., CuO/Cu based superhydrophobic and self-cleaning surfaces. *Scripta Materialia* **2016,** *118*, 60-64.
7. Zhu, Q.; Li, B.; Li, S.; Luo, G.; Zheng, B.; Zhang, J., Superamphiphobic Cu/CuO Micropillar Arrays with High Repellency Towards Liquids of Extremely High Viscosity and Low Surface Tension. *Sci Rep* **2019,** *9* (1), 702.
8. Vereecken, P. M.; Binstead, R. A.; Deligianni, H.; Andricacos, P. C., The chemistry of additives in damascene copper plating. *IBM J. Res. & Dev.* **2005,** *49* (1), 3 - 18.
9. Moffat, T. P.; Josell, D., Extreme bottom-up superfilling of through-silicon-vias by damascene processing. *Journal of The Electrochemical Society* **2012,** *159* (4), D208 - D216.
10. Walsh, F. C.; Herron, M. E., Electrocrystallization and electrochemical control of crystal growth: Fundamental considerations and electrodeposition of metals. *Journal of Physics D: Applied Physics* **1991,** *24*, 217-225.
11. Dini, J. W.; Snyder, D. D., *Modern Electroplating*. 5th ed.; John Wiley & Sons, Inc.: 2010.
12. Hai, N. T. M.; Huynh, T. T. M.; Fluegel, A.; Arnold, M.; Mayer, D.; Reckien, W.; Bredow, T.; Broekmann, P., Competitive anion/anion interactions on copper surfaces relevant for Damascene electroplating. *Electrochimica Acta* **2012,** *70*, 286-295.
13. Huynh, T. M. T.; Weiss, F.; Hai, N. T. M.; Reckien, W.; Bredow, T.; Fluegel, A.; Arnold, M.; Mayer, D.; Keller, H.; Broekmann, P., On the role of halides and thiols in additive-assisted copper electroplating. *Electrochimica Acta* **2013,** *89*, 537-548.
14. Chrzanowska, A.; Mroczka, R., Influence of chloride anions and polyethylene glycol on the morphology of electrodeposited copper layers. *Electrochimica Acta* **2012,** *78*, 316-323.
15. Sebastián, P.; Torralba, E.; Vallés, E.; Molina, A.; Gómez, E., Advances in Copper Electrodeposition in Chloride Excess. A Theoretical and Experimental Approach. *Electrochimica Acta* **2015,** *164*, 187-195.
16. Schneider, N. M.; Park, J. H.; Grogan, J. M.; Steingart, D. A.; Bau, H. H.; Ross, F. M., Nanoscale evolution of interface morphology during electrodeposition. *Nat Commun* **2017,** *8* (1), 2174.

17. Orhan, G.; Hapçı, G., Effect of electrolysis parameters on the morphologies of copper powder obtained in a rotating cylinder electrode cell. *Powder Technology* **2010,** *201* (1), 57-63.
18. Cao, H.; Wang, L.; Qiu, Y.; Zhang, L., Synthesis and I-V properties of aligned copper nanowires. *Nanotechnology* **2006,** *17* (6), 1736-9.
19. Chen, X.; Duan, H.; Zhou, Z.; Liang, J.; Gnanaraj, J., Fabrication of free-standing Cu nanorod arrays on Cu disc by template-assisted electrodeposition. *Nanotechnology* **2008,** *19* (36), 365306.
20. Maurer, F.; Brotz, J.; Karim, S.; Toimil Molares, M. E.; Trautmann, C.; Fuess, H., Preferred growth orientation of metallic fcc nanowires under direct and alternating electrodeposition conditions. *Nanotechnology* **2007,** *18* (13), 135709.
21. Quemper, J.-M.; Dufour-Gergam, E.; Frantz-Rodriguez, N.; Gilles, J.-P.; Grandchamp, J.-P.; Bosseboeuf, A., Effects of direct and pulse current on copper electrodeposition through photoresist molds. *Journal of Micromechanics and Microengineering* **2000,** *10*, 116-119.
22. Bard, A. J.; Faulkner, L. R., *Electrochemical methods - Fundamentals and applications*. 2nd ed.; John Wiley & Sons, Inc.: 2001.
23. Bazant, M. Z.; Thornton, K.; Ajdari, A., Diffuse-charge dynamics in electrochemical systems. *Phys Rev E Stat Nonlin Soft Matter Phys* **2004,** *70* (2 Pt 1), 021506.
24. Tao, S.; Li, D. Y., Tribological, mechanical and electrochemical properties of nanocrystalline copper deposits produced by pulse electrodeposition. *Nanotechnology* **2006,** *17* (1), 65-78.
25. Tsai, W.-C.; Wan, C.-C.; Wang, Y.-Y., Mechanism of copper electrodeposition by pulse current and its relation to current efficiency. *Journal of Applied Electrochemistry* **2002,** *32* (1371-1378).
26. Pavithra, C. L. P.; Sarada, B. V.; Rajulapati, K. V.; Ramakrishna, M.; Gundakaram, R. C.; Rao, T. N.; Sundararajan, G., Controllable Crystallographic Texture in Copper Foils Exhibiting Enhanced Mechanical and Electrical Properties by Pulse Reverse Electrodeposition. *Crystal Growth & Design* **2015,** *15* (9), 4448-4458.
27. Brown, D. A.; Morgan, S.; Peldzinski, V.; Brüning, R., Crystal growth patterns in DC and pulsed plated galvanic copper films on (1 1 1), (1 0 0) and (1 1 0) copper surfaces. *Journal of Crystal Growth* **2017,** *478*, 220-228.
28. Natter, H.; Hempelmann, R., Nanocrystalline copper by pulsed electrodeposition. *Journal of Physical Chemistry* **1996,** *100*, 19525-19532.
29. Lui, G.-T.; Chen, D.; Kuo, J.-C., EBSD characterization of twinned copper using pulsed electrodeposition. *Journal of Physics D: Applied Physics* **2009,** *42* (21), 215410.
30. Mieszala, M.; Guillonneau, G.; Hasegawa, M.; Raghavan, R.; Wheeler, J. M.; Mischler, S.; Michler, J.; Philippe, L., Orientation-dependent mechanical behaviour of electrodeposited copper with nanoscale twins. *Nanoscale* **2016,** *8* (35), 15999-6004.
31. Xu, L.; Dixit, P.; Miao, J.; Pang, J. H. L.; Zhang, X.; Tu, K. N.; Preisser, R., Through-wafer electroplated copper interconnect with ultrafine grains and high density of nanotwins. *Applied Physics Letters* **2007,** *90* (3), 033111.
32. Zhu, Q. S.; Zhang, X.; Liu, C. Z.; Liu, H. Y., Effect of reverse pulse on additives adsorption and copper filling for through silicon via. *Journal of The Electrochemical Society* **2019,** *166* (1), D3006-D3012.
33. Shao, W.; Pattanaik, G.; Zangari, G., Influence of Chloride Anions on the Mechanism of Copper Electrodeposition from Acidic Sulfate Electrolytes. *Journal of The Electrochemical Society* **2007,** *154* (4), D201.
34. Yanson, Y. I.; Rost, M. J., Structural accelerating effect of chloride on copper electrodeposition. *Angew Chem Int Ed Engl* **2013,** *52* (9), 2454-8.
35. Lafouresse, M. C.; Heard, P. J.; Schwarzacher, W., Surface roughness analysis of electrodeposited Cu. *Electrochimica Acta* **2007,** *53* (1), 229-232.
36. Nikolić, N. D.; Branković, G.; Maksimović, V. M.; Pavlović, M. G.; Popov, K. I., Influence of potential pulse conditions on the formation of honeycomb-like copper electrodes. *Journal of Electroanalytical Chemistry* **2009,** *635* (2), 111-119.
37. Cheng, J. J.; Nicaise, S. M.; Berggren, K. K.; Gradecak, S., Dimensional Tailoring of Hydrothermally Grown Zinc Oxide Nanowire Arrays. *Nano Lett* **2016,** *16* (1), 753-9.

38. Gründer, Y.; Drünkler, A.; Golks, F.; Wijts, G.; Stettner, J.; Zegenhagen, J.; Magnussen, O. M., Structure and electrocompression of chloride adlayers on Cu(111). *Surface Science* **2011,** *605* (17-18), 1732-1737.
39. Broekmann, P.; Wilms, M.; Kruft, M.; Stuhlmann, C.; Wandelt, K., In-situ STM investigation of specific anion adsorption on Cu(111). *Journal of Electroanalytical Chemistry* **1999,** *467*, 307-324.
40. Polewska, W.; Behm, R. J.; Magnussen, O. M., In-situ video-STM studies of Cu electrodeposition on Cu(100) in HCl solution. *Electrochimica Acta* **2003,** *48* (20-22), 2915-2921.
41. Kozhummal, R.; Yang, Y.; Guder, F.; Hartel, A.; Lu, X.; Kucukbayrak, U. M.; Mateo-Alonso, A.; Elwenspoek, M.; Zacharias, M., Homoepitaxial branching: An unsual polymorph of zinc oxide derived from seeded solution growth. *ACS Nano* **2012,** *6* (8), 7133 - 7414.
42. McCrum, I. T.; Akhade, S. A.; Janik, M. J., Electrochemical specific adsorption of halides on Cu 111 , 100 , and 211 : A Density Functional Theory study. *Electrochimica Acta* **2015,** *173*, 302-309.
43. Thermal conductivity of metals. www.engineeringtoolbox.com (accessed 11/11/2019).
44. Thermal contact resistance. www.neutrium.net/heat_transfer/thermal-contact-resistance/ (accessed 11/11/2019).

TOC Graphic